

PCCP

Accepted Manuscript



This is an *Accepted Manuscript*, which has been through the Royal Society of Chemistry peer review process and has been accepted for publication.

Accepted Manuscripts are published online shortly after acceptance, before technical editing, formatting and proof reading. Using this free service, authors can make their results available to the community, in citable form, before we publish the edited article. We will replace this *Accepted Manuscript* with the edited and formatted *Advance Article* as soon as it is available.

You can find more information about *Accepted Manuscripts* in the [Information for Authors](#).

Please note that technical editing may introduce minor changes to the text and/or graphics, which may alter content. The journal's standard [Terms & Conditions](#) and the [Ethical guidelines](#) still apply. In no event shall the Royal Society of Chemistry be held responsible for any errors or omissions in this *Accepted Manuscript* or any consequences arising from the use of any information it contains.

**In situ synthesis of hierarchical CoFe₂O₄ nanoclusters/graphene aerogels and
their high performance for lithium-ion batteries**

Beibei Wang^a, Gang Wang^b, Zhengyuan Lv^a, Hui Wang^{a*}

^aKey Laboratory of Synthetic and Natural Functional Molecule Chemistry (Ministry of Education), College of Chemistry & Materials science, Northwest University, Xi'an 710127, PR China

^bNational Key Laboratory of Photoelectric Technology and Functional Materials (Culture Base), National Photoelectric Technology and Functional Materials & Application International Cooperation Base, Institute of Photonics & Photon-Technology, Northwest University, Xi'an 710069, PR China

*Corresponding author:

Tel.: +86 29 8836 3115

Fax: +86 29 8830 3798

E-mail address: huiwang@nwu.edu.cn (H. Wang)

Abstract

In this article, we demonstrate a simple solvothermal method towards in situ growth of hierarchical CoFe_2O_4 nanoclusters on graphene aerogels (GAs). SEM and TEM results confirm that CoFe_2O_4 nanoclusters are well wrapped by the graphene. As an anode material for lithium-ion batteries, $\text{CoFe}_2\text{O}_4/\text{GAs}$ composite displays a stable cycling performance with a reversible capacity of after 100 discharge/charge cycles at the current density of 0.1 A g^{-1} , much higher than that of CoFe_2O_4 nanoclusters. Moreover, the reversible capacity of $\text{CoFe}_2\text{O}_4/\text{GAs}$ composite exhibits 966 mAh g^{-1} after 300 cycles even at a high current density of 0.5 A g^{-1} . Most important of all, a new $\text{CoFe}_2\text{O}_4/\text{GAs}/\text{LiCoO}_2$ full cell was successfully assembled, and exhibited excellent electrochemical performance. The superior electrochemical performance of the $\text{CoFe}_2\text{O}_4/\text{GAs}$ composite in half and full cells can be attributed to the synergistic interaction between the uniform CoFe_2O_4 nanoclusters and GAs, the high electrical conductivity, and three-dimensional hierarchically porous structure, which can not only facilitate the diffusion of Li ions and electrolyte into the electrodes, but also prevent volume expansion/contraction upon prolonged discharge/charge cycling.

Keywords: $\text{CoFe}_2\text{O}_4/\text{GAs}$ composite; solvothermal; anode material; electrochemical performance

1. Introduction

Lithium-ion batteries (LIBs) have become the predominant power source for portable electronics, smart grids, plugging hybrid EVs, and so forth.^{1,2} The ever-increasing market demands for LIBs have greatly stimulated extensive research into advanced electrode materials with higher energy and power densities.^{3,4} Transition metal oxides (TMOs), such as Fe_3O_4 , NiO , Co_3O_4 and CuO , have been considered as alternative potential alternatives for anode materials due to their high theoretical capacities and natural abundance.⁵⁻⁹ Besides these simple TMOs, considerable research efforts have been focused on developing novel ternary oxides. Recently, Fe-based TMOs with a spinel structure (e. g. NiFe_2O_4 , CuFe_2O_4 , ZnFe_2O_4) have recently attracted significant research interest owing to the synergic effects of multiple metal species and their complex chemical composition, which have shown much enhanced LIBs performance.¹⁰⁻¹² Among a variety of candidates, ternary CoFe_2O_4 has been well regarded as a distinguished anode in view of its low cost, high chemical stability and good environmental benignity. Importantly, CoFe_2O_4 possesses a high theoretical capacity of 914 mAh g^{-1} , which is about three-times higher than that of the conventional graphite-based materials.¹³ Regrettably, like other TMOs, the intrinsic poor electric conductivity and electrode pulverization induced by huge volume variations and particle aggregation during cycling process can lead to dramatic capacity fading, poor cycling stability and rate capability.^{14,15} It is greatly hampered the practical application of CoFe_2O_4 -based electrodes. To address these problems, many strategies have been developed significantly. One potential strategy is to design CoFe_2O_4 with various morphologies on the nanoscale (such as nanosheets, nanospheres, nanotubes and nanorods).¹⁶⁻¹⁹ These nanostructured materials are beneficial to shorten the lithium ion diffusion distance and buffer the mechanical

strain during cycles. Another effective strategy is to construct hybrid electrodes composed of CoFe_2O_4 and carbon materials (graphene, carbon nanotubes, graphitic carbon, etc.), thus improving the conductivity and providing rapid electron channel.²⁰

Graphene is an intriguing two-dimensional material and has attracted great research interest due to its outstanding characteristics, including large surface area, chemical and thermal stability and high electric conductivity.^{21,22} Importantly, graphene can not only improve the electric conductivity, but also prevent self-aggregation and volume expansion/extraction of nanoparticles during the cycling process.²³ So far, intensive efforts have been devoted to preparing graphene-based transition metal oxide composites, which exhibited a great improvement in their electrochemical performance of high lithium storage capability.²⁴⁻²⁷ Compared with two-dimensional (2D) graphene, three-dimensional (3D) graphene aerogels (GAs) have attracted much more attention due to its unique 3D interconnected framework, high surface area, fast mass and electron transport rate and good flexibility.²⁸ Therefore, it is still desirable to develop a simple method to achieve 3D hierarchical $\text{CoFe}_2\text{O}_4/\text{GAs}$ composite with longer cycling life and higher rate performance.

Herein, we demonstrate a simple one-step solvothermal method for in situ preparation of hierarchical $\text{CoFe}_2\text{O}_4/\text{GAs}$. This unique structure of the obtained $\text{CoFe}_2\text{O}_4/\text{GAs}$ composite cannot only effectively prevent the aggregation of CoFe_2O_4 nanoclusters but also greatly improve the electronic conductivity compared to the independent CoFe_2O_4 nanoclusters. When evaluated as an anode material in half cells for LIBs, the $\text{CoFe}_2\text{O}_4/\text{GAs}$ composite exhibits a high reversible capacity of 1070 mAh g^{-1} at 0.1 A g^{-1} after 100 cycles. In order to prove the feasibility practical applications of $\text{CoFe}_2\text{O}_4/\text{GAs}$ composite, full cells were assembled by using commercial lithium cobalt oxides (LiCoO_2) cathode and $\text{CoFe}_2\text{O}_4/\text{GAs}$ as the anode.

To the best of our knowledge, there is still no published study using CoFe₂O₄/GAs composite as anode in full cells. The CoFe₂O₄/GAs//LiCoO₂ full cell also exhibits a relatively high capacity of 803 mAh g⁻¹ at 0.1 A g⁻¹ over 50 cycles. The remarkable electrochemical performance in both half and full cells demonstrate that hierarchical CoFe₂O₄/GAs composite has potential applications in high performance LIBs.

2. Experimental

2.1 Synthesis of CoFe₂O₄/GAs composite

Graphite oxide (GO) was synthesized from commercial graphite using a modified Hummers method.²⁹ In a typical procedure, 1.4 mmol of FeCl₃·6H₂O and 0.7 mmol of CoCl₂·6H₂O were dissolved in GO solution (45 mg of GO was dispersion in 20 ml Ethylene glycol solution) under stirring for 30 min. Then 100 mg sodium citrate and 600 mg sodium acetate was slowly added to form a stable complex solution. After mechanical stirring for 30 min, the resulting suspension was transferred into a 40 ml Teflon-lined stainless autoclave, sealed and maintained at 200 °C for 12 h. After cooling to room temperature, the obtained CoFe₂O₄/GAs was washed with deionized water and ethanol several times, and freeze dried. As a reference, pure CoFe₂O₄ nanoclusters were prepared using with the same experimental condition without GO.

2.2 Material Characterization

X-ray powder diffraction (XRD) patterns were recorded using a diffractometer (Rigaku) with Cu K_α radiation at a scanning step of 0.03° s⁻¹ in the 2θ range from 10 to 80°. Morphology features of the obtained materials were investigated by field scanning electron microscopy (SEM, FEI Quanta 400 ESEM-FEG) and high-resolution transmission electron microscopy (TEM, JEOL JEM-3010). Raman spectra were conducted on a Nicolet Almega dispersive Raman spectrometer with 532 nm laser excitation. X-ray photoelectron spectroscopy (XPS) was determined on a

PHI-5400 electron spectrometer with Mg K_a X-ray as the excitation source. The surface area and pore size distribution were determined by nitrogen adsorption through Brunauer-Emmett-Teller (BET) and Barrett-Joyner-Halenda (BJH) methods. Thermogravimetric analysis (TGA, Q 600) was carried out from room temperature to 800 °C under an air flow with a heating rate of 10 °C min⁻¹.

2.3 Electrochemical measurements

The electrochemical properties of materials for half cells were carried out using CR2025 coin-type cells and lithium foil was used as the counter electrode. The working electrodes were obtained by mixing active materials, acetylene black and polyvinylidene fluoride (PVDF) at a weight ratio of 80:10:10, and dissolved in N-methyl-2-pyrrolidinone (NMP). Then, the obtained slurries were spread on nickel foam with 14 mm diameter and dried at 100 °C for 12 h under vacuum to remove the solvent. The mass loading on each current collector is about 2 mg cm⁻². The electrolyte solution was 1 M LiPF₆ dissolved in a mixture of dimethyl carbonate (DMC), diethyl carbonate (DEC) and ethylene carbonate (EC) (1:1:1 by volume). The separator was microporous polypropylene membrane. In addition, the coin-type full cells were fabricated by using the CoFe₂O₄/GAs composite as the anode, the commercial LiCoO₂ as the cathode. The other conditions were the same as those used for half cells. Before constructing full cell, the CoFe₂O₄/GAs anode was electrochemically activated for in half-cell at a current rate of 0.1 A g⁻¹, and then the cell was disassembled and re-collected in a full cell. The fabricated full cell was slightly anode limited and cycled at 0.1 A g⁻¹. All the test cells were assembled in a glove box filled with high-purity argon. All galvanostatic discharge/charge tests were conducted on a LAND CT 2001A battery system tester at various current rates in a cut-off voltage window of 0.005-3.0 V for the half cells and 1-3.8 V for the full cells.

Cyclic voltammetry (CV) experiments were recorded using a CHI 660D electrochemical workstation at a scanning rate of 0.1 mV s^{-1} . Electrochemical impedance spectroscopy (EIS) measurements were carried on the same electrochemical workstation over the frequency range between 100 kHz and 0.01 Hz.

3. Results and discussion

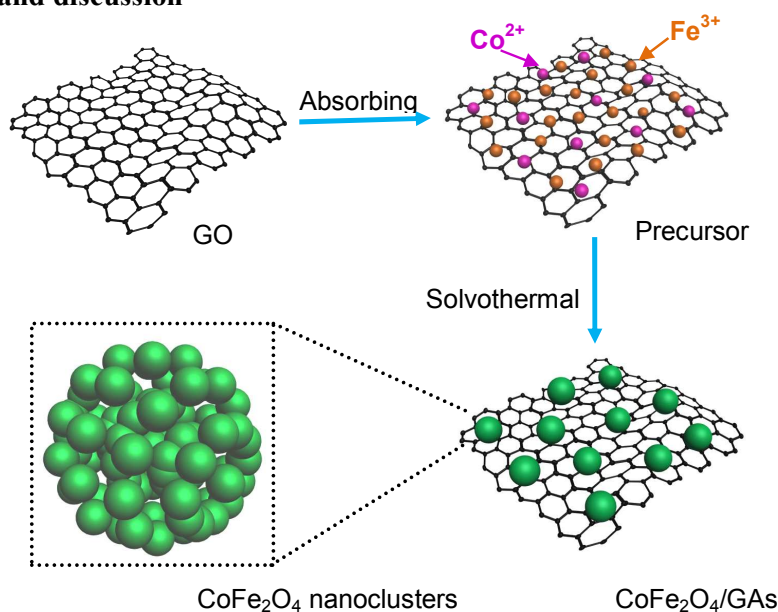


Fig. 1 Schematic illustration of the synthesis of the CoFe₂O₄/GAs composite.

Synthesis of CoFe₂O₄/GAs composite is illustrated in Fig. 1. Firstly, Fe^{3+} and Co^{2+} cations are adsorbed onto the surface of GO sheets due to electrostatic interactions. Secondly, CoFe₂O₄ nanoclusters were grown on the surface accompanied with reduction of GO to GAs under a solvothermal treatment. Finally, black CoFe₂O₄/GAs was obtained after the freeze drying process. The XRD patterns of bare CoFe₂O₄ nanoclusters and CoFe₂O₄/GAs composite are shown in Fig. 2a. It can be clearly seen that the CoFe₂O₄/GAs shows similar diffraction peaks to the CoFe₂O₄. The five main characteristic diffraction peaks at 30.1 , 35.4 , 43.1 , 57.0 and 62.6° are ascribed to the (220), (311), (400), (511) and (440) planes of a face-centered cubic spinel CoFe₂O₄ (JCPDS No. 22-1086) with the Fd3m space group.³⁰ No typical diffraction peaks of

GO (Fig. S1) are observable in the XRD pattern of the composite, which indicates the successful reduction of GO during the synthesis process. Additionally, no obvious diffraction peak at 26° corresponding to graphene was detected in the $\text{CoFe}_2\text{O}_4/\text{GAs}$ composite, suggesting that the graphene sheets are well-separated by numerous CoFe_2O_4 nanoclusters.^{30,31} The results confirmed that CoFe_2O_4 was successfully formed on GAs by the solvothermal method.

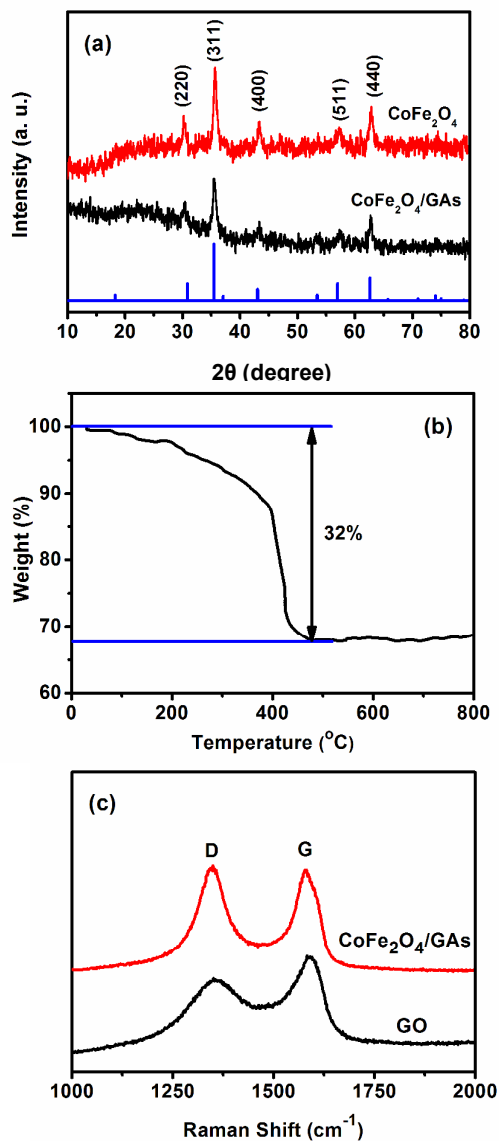


Fig. 2 (a) XRD patterns of CoFe_2O_4 nanoclusters and $\text{CoFe}_2\text{O}_4/\text{GAs}$ composite. (b) TGA profiles of $\text{CoFe}_2\text{O}_4/\text{GAs}$ composite. (c) Raman spectra of GO and $\text{CoFe}_2\text{O}_4/\text{GAs}$ composite.

TG analysis was carried out to calculate the amount of carbon present in the $\text{CoFe}_2\text{O}_4/\text{GAs}$ composite. According to the TG result (Fig. 2b), the weight of graphene sheets in the composite was estimated to be about 32%. Raman spectra of GO and $\text{CoFe}_2\text{O}_4/\text{GAs}$ composite are shown in Fig. 2c. The two samples show the D band at approximately 1349 cm^{-1} and the G band at approximately 1583 cm^{-1} . Notably, the I_D/I_G ratios were 0.80 and 1.02 for GO and GAs . The higher I_D/I_G ratio of $\text{CoFe}_2\text{O}_4/\text{GAs}$ is attributed to a increase number of sp^2 domains during the reduction reactions, confirming the successfully reduction of GO.³²

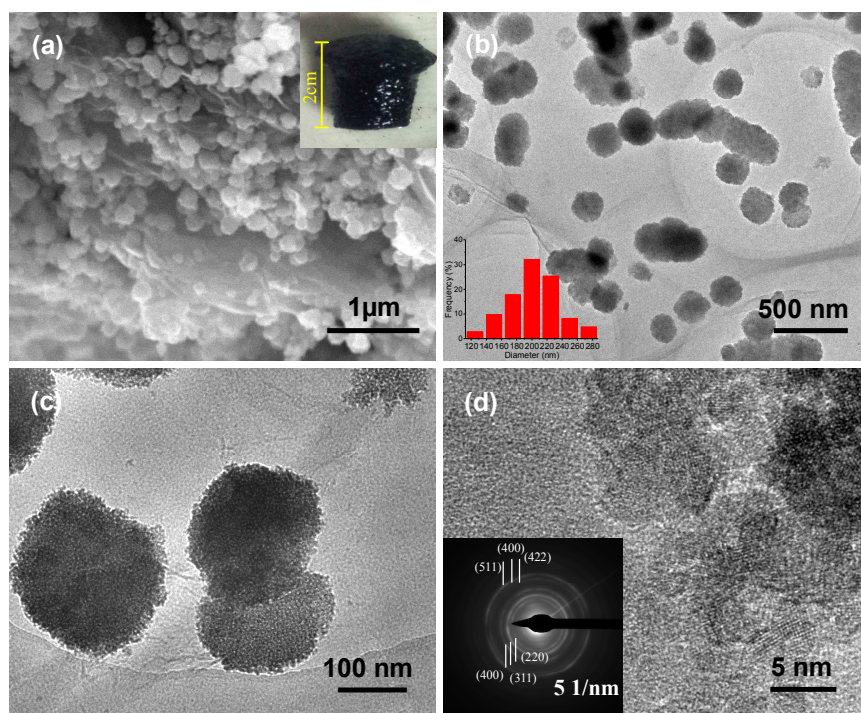


Fig. 3 (a) SEM image of the $\text{CoFe}_2\text{O}_4/\text{GAs}$ composite. (b-d) TEM and HRTEM images of $\text{CoFe}_2\text{O}_4/\text{GAs}$ composite. Inset of (a) is a digital photo of the resulting $\text{CoFe}_2\text{O}_4/\text{GAs}$ composite. Inset of (b) is the diameter distribution of CoFe_2O_4 . Inset of (d) is the corresponding SAED pattern of CoFe_2O_4 .

The morphology and microstructure of $\text{CoFe}_2\text{O}_4/\text{GAs}$ and CoFe_2O_4 were investigated by SEM, TEM, and high resolution TEM (HRTEM). As shown in Fig. 3a,

CoFe₂O₄ nanoclusters are uniformly distributed within the graphene matrix and well wrapped by the stacked graphene. The CoFe₂O₄ nanoclusters in the CoFe₂O₄/GAs composite perform a uniform size distribution from 150 nm up to 250 nm, which is similar to that of pure CoFe₂O₄ nanoclusters (Fig. S2a). The inset in Fig. 2a shows a digital photo of the resulting CoFe₂O₄/GAs composite. From it one can see that the composite displays an aerogel state. A typical EDS spectrum from Fig. S3b suggests the presence of C, Fe, Co, and O elements in the as-prepared CoFe₂O₄/GAs composite, which is consistent with the XRD analysis. The Cu peak is induced by the spattering Cu metal used for SEM analysis. The corresponding elemental mapping images (Fig. S3c-f) demonstrate that C, Fe, Co and O elements are homogeneously distributed over the composite. Moreover, the TEM images (Fig. 3b and c) reveal that CoFe₂O₄ nanoclusters are well distributed on the graphene. The diameter distribution of CoFe₂O₄ nanoclusters was measured, as shown in the inset of Fig. 3b, and the average size is mainly within the range of 150-250 nm. The HRTEM image in Fig. 3d clearly suggests that CoFe₂O₄ nanoclusters are made up of many numbers of small CoFe₂O₄ nanoparticles (5 nm). Obviously, CoFe₂O₄ nanoclusters have porous structure and the lattice is clear. The inset of Fig. 3d shows a very light ring-pattern of SAED. The diffraction rings can be indexed to (220), (311), (400), (422), (511) and (440) planes of CoFe₂O₄, which are in accordance with the XRD analysis.

The chemical composition and valence state of the obtained CoFe₂O₄/GAs composite were examined by XPS. As shown in Fig. 4a, signals of Co, Fe, C as well as O can be identified from the survey spectrum. The peaks centered at 782.7 and 796.8 eV in Fig. 4b are assigned to Co 2p_{3/2} and Co 2p_{1/2}, respectively. The satellite peaks at 788.5 and 785.9 eV are two shake-up type peaks of Co at the high binding energy side of the Co 2p_{3/2} and Co 2p_{1/2} edge, which demonstrate the presence of Co²⁺

in the sample.³³ The Fe 2p spectrum in Fig. 4c shows that the peaks at binding energy of 710.6 and 717.2 eV correspond to Fe 2p_{3/2} and its shakeup satellites, respectively, and those at 724.9 and 732.8 eV correspond to Fe 2p_{1/2} and its shakeup satellites, respectively.³⁴ The presence of the satellite peaks in Fig. 4c confirms the chemical state of Fe³⁺. The major peak located at 284.0 eV for C 1s is assigned to C=C and C-C of aromatic rings (Fig. 4d). The other weaker peaks are related to the C-O bond (285.2 eV), the carbonyl group (C=O, 286.1 eV) and the carboxyl group (O-C=O, 287.5 eV).³⁵ The result proves that most of the oxygen-containing groups are removed after the solvothermal process. Moreover, the high-resolution spectrum for O 1s shows the oxygen contribution (Fig. 4e). The XPS results strongly indicate that the as-synthesized composite is composed of CoFe₂O₄ and GAs, which is consistent with the XRD results. The BET specific surface area and pore size distribution of the CoFe₂O₄/GAs composite were investigated by nitrogen adsorption-desorption measurement. As shown in Fig. 4f, the BET specific surface area of CoFe₂O₄/GAs composite is calculated to be 185.4 m² g⁻¹, which is much higher than that of pure CoFe₂O₄ (38.3 m² g⁻¹, Fig. S4). The pore size for CoFe₂O₄/GAs (inset in Fig. 4d) is mainly in the range of 4-5 nm, which contributes to the pores existing between the CoFe₂O₄ nanoparticles. The wide pores size distribution from 50 nm to 120 nm attribute to the pores existing between CoFe₂O₄ nanoclusters and 3D graphene. Combining the result with TEM measurement, the hierarchical porous structure demonstrates that the synergistic effect of mesopores and macropores may permit easy access for electrons and ions to the electrode/electrolyte and accommodate the volume change of the CoFe₂O₄ nanoclusters during discharge/charge cycles. This feature should be beneficial to realize the material with high lithium storage property.

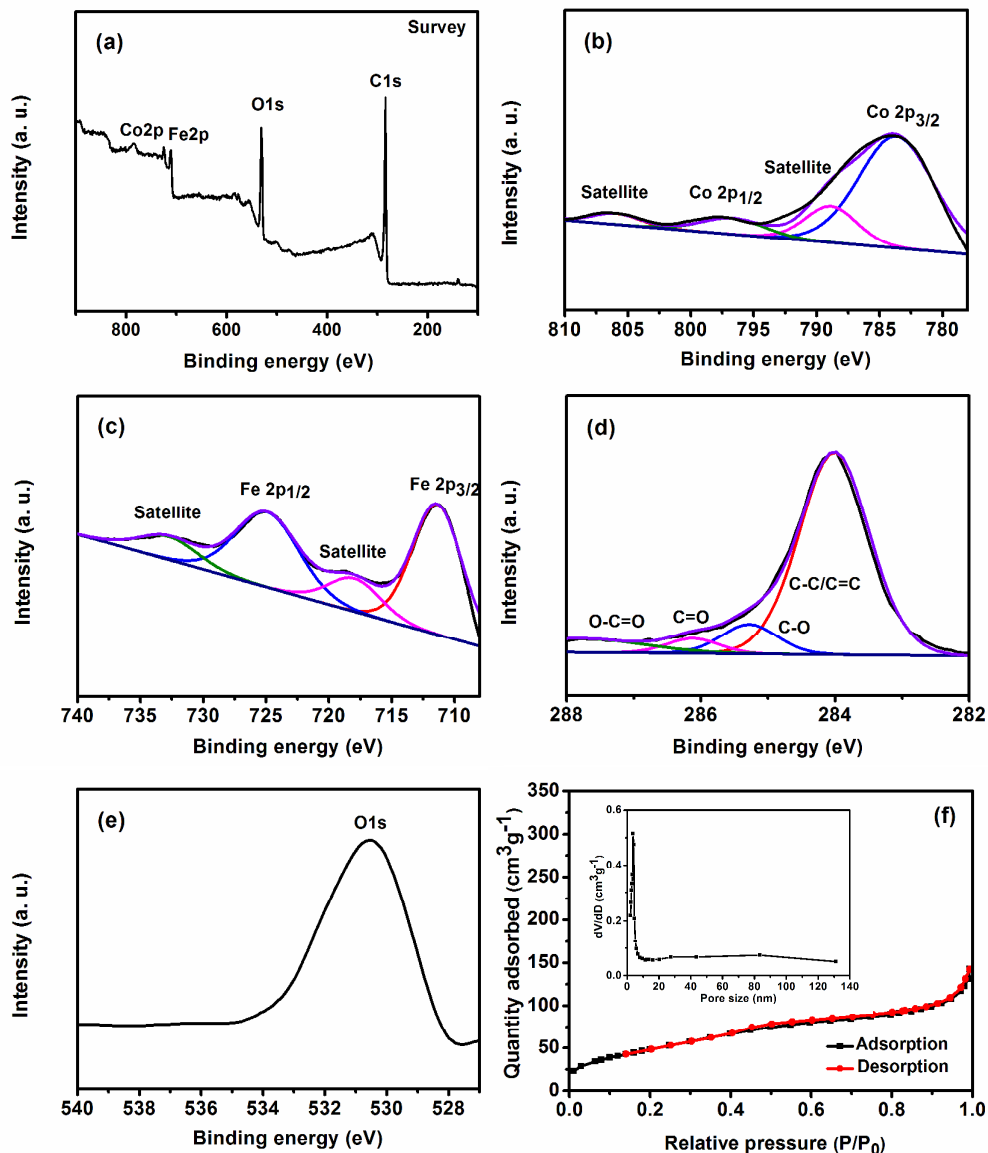


Fig. 4 XPS spectra of CoFe₂O₄/GAs composite: (a) survey spectrum, (b) Co 2p spectrum, (c) Fe 2p spectrum, (d) C1s spectrum, (e) O 1s spectrum, and (f) Nitrogen adsorption/desorption isotherms and corresponding BJH pore size distribution curve of CoFe₂O₄/GAs composite.

The electrochemical performance of the as-synthesized CoFe₂O₄/GAs composite as anode material for LIBs was first investigated in a half-cell test. Fig. 5a shows the first three cycles of CV curves of the CoFe₂O₄/GAs electrode at a scan rate of 0.1 mA s⁻¹ in the potential range from 3 to 0 V vs Li/Li⁺. The CV curves of the CoFe₂O₄

electrode can be found in Fig. S5a. In the first cathodic process, two peaks appeared at approximately 0.59 V and 1.52 V is attributed to the conversion reactions of Fe^{3+} and Co^{2+} to their metallic states and the formation of an solid electrolyte interphase (SEI) layer by the reaction $\text{CoFe}_2\text{O}_4 + 8\text{Li}^+ + 8\text{e}^- \rightarrow 2\text{Fe} + \text{Co} + 4\text{Li}_2\text{O}$.³⁶ In the first anodic scan, the broad peak at approximately 1.6-1.9 V can be attributed to the reversible oxidations $\text{Fe}^0 \rightarrow \text{Fe}^{3+}$ and $\text{Co}^0 \rightarrow \text{Co}^{2+}$, respectively. In the second cycle, the cathodic peaks shift to approximately 0.75 V and 1.4 V, while the anodic process is almost without changes. The significance difference between the peaks in the 1st and the following cycles is related to activation processes, which causes a degree of irreversible capacity loss in the first discharge and charge process.³⁵

Fig. 5b shows the discharge and charge profiles of the $\text{CoFe}_2\text{O}_4/\text{GAs}$ composite for different cycles at a current density of 0.1 A g^{-1} with a voltage range of 0.005-3 V. The initial discharge curve of the $\text{CoFe}_2\text{O}_4/\text{GAs}$ composite exhibits a long voltage plateau at $\sim 0.75 \text{ V}$, followed by sloping down to the cut-off voltage of 0.005 V. In the subsequent discharge steps, the plateau shifts to 1.4-0.8 V, corresponds to the reduction reaction. The broad plateau around 1.6-1.9 in the charge steps can be ascribed to the oxidation of Fe to Fe^{3+} and Co to Co^{2+} , which showed no obviously shift in the subsequent cycles. The reaction can be described as: $\text{Co} + 2\text{Fe} + 4\text{Li}_2\text{O} = \text{CoO} + \text{Fe}_2\text{O}_3 + 8\text{Li}^+ + 8\text{e}^-$. The initial discharge and charge capacities of $\text{CoFe}_2\text{O}_4/\text{GAs}$ composite are 1828 and 1221 mAh g^{-1} , with an initial coulombic efficiency of 67%. However, the initial discharge and charge capacities of CoFe_2O_4 are only 1336 and 789 mAh g^{-1} (Fig. S5b). Accordingly, the coulombic efficiency of CoFe_2O_4 electrode can be calculated to be 59%, which is lower than the result obtained from $\text{CoFe}_2\text{O}_4/\text{GAs}$ electrode. The irreversible capacity loss and low coulombic efficiency for both electrodes in the first discharge/charge process could be

attributed to the formation of SEI layer on the surface of the electrode, which is commonly observed in most anode materials.³⁷ Compared to the theoretical capacity of CoFe_2O_4 (916 mAh g^{-1}) and graphene (744 mAh g^{-1}),^{38,39} the extra reversible capacity may be attributed to the formation of a pseudo-capacitive gel like film, which have been observed before for other metal oxide anodes.⁴⁰ In the subsequent cycles, the discharge/charge capacity of $\text{CoFe}_2\text{O}_4/\text{GAs}$ decreases slightly, while the capacity of pure CoFe_2O_4 decreases obviously. This result implies $\text{CoFe}_2\text{O}_4/\text{GAs}$ could exhibit higher initial capacities and better reversibility than pure CoFe_2O_4 .

The cycling performance of $\text{CoFe}_2\text{O}_4/\text{GAs}$ and CoFe_2O_4 at current density of 0.1 A g^{-1} are shown in Fig. 5c. It can be seen that the reversible capacity of $\text{CoFe}_2\text{O}_4/\text{GAs}$ electrode is 1070 mAh g^{-1} after 100 cycles, and the coulombic efficiency remains 100% upon cycling. Unsurprisingly, CoFe_2O_4 electrode exhibits much lower reversible capacity and faster capacity fading. It can be clearly seen that the capacity of the pure CoFe_2O_4 decreases to 473 mA h g^{-1} after 100 cycles at the current density of 0.1 A g^{-1} . The specific reversible capacity of 1070 mAh g^{-1} after 100 cycles for $\text{CoFe}_2\text{O}_4/\text{GAs}$ is 2.2 times higher than that of pure CoFe_2O_4 and 3 times greater as compared to the theoretical capacity of graphite (372 mAh g^{-1}). Most notably, the capacity and cycle performance of $\text{CoFe}_2\text{O}_4/\text{GAs}$ composite is much better than those of the previously reported $\text{CoFe}_2\text{O}_4/\text{carbon}$ anode materials, such as $\text{CoFe}_2\text{O}_4/\text{nanotube}$, $\text{CoFe}_2\text{O}_4/\text{C}$, and $\text{CoFe}_2\text{O}_4/\text{graphene}$, etc. (Table S1).^{30,41-47} The greatly enhanced cycle stability of the $\text{CoFe}_2\text{O}_4/\text{GAs}$ electrode can be attributed to the synergistic effect between CoFe_2O_4 and GAs. The GAs can effectively prevent the volume change and aggregation of CoFe_2O_4 electrode during the repeated Li^+ insertion/extraction processes. Meanwhile, the CoFe_2O_4 nanoclusters uniformly distributed within the graphene matrix can reduce the restacking of the neighboring

graphene sheets.

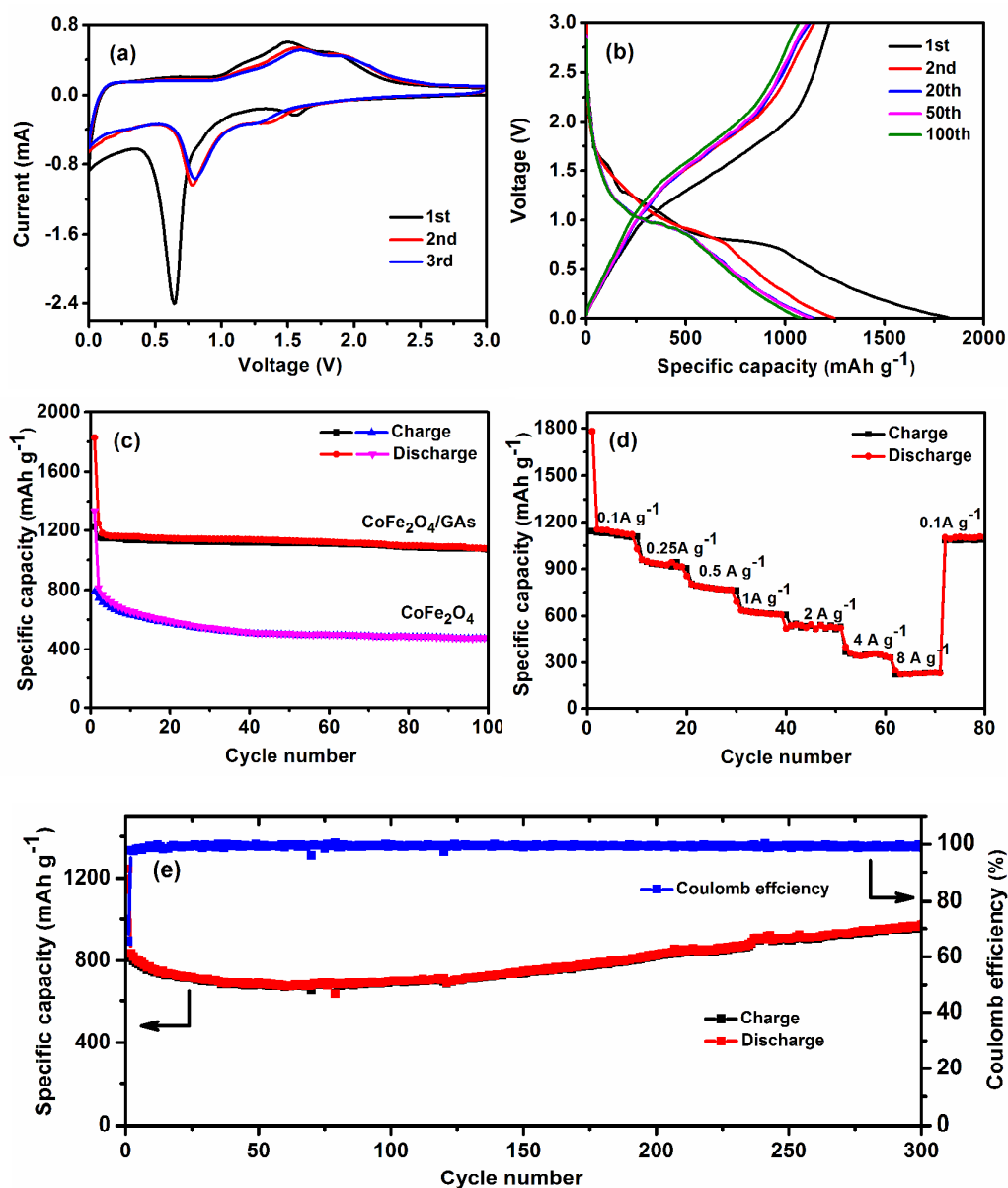


Fig. 5 (a) CV profiles of the CoFe₂O₄/GAs electrode at a scan rate of 0.1 mV s⁻¹. (b) Discharge/charge profiles of the CoFe₂O₄/GAs electrode. (c) Cycle performance of the CoFe₂O₄/GAs and CoFe₂O₄ electrodes at a current density of 0.1 A g⁻¹. (d) Rate capabilities of the CoFe₂O₄/GAs electrode. (e) Long-term cycle performance of the CoFe₂O₄/GAs electrode at a current density of 0.5 A g⁻¹.

The rate capabilities of the as-prepared CoFe₂O₄/GAs electrode were evaluated by

discharge/charge experiments at various current densities, as shown in Fig. 5d. With the increasing current densities from 0.1 to 8 A g⁻¹, the corresponding average reversible capacities of CoFe₂O₄/GAs electrode are 1124, 924, 776, 616, 534, 341 and 221 mAh g⁻¹ at 0.1, 0.2, 0.5, 1, 2, 4 and 8 A g⁻¹, respectively. Notably, the reversible capacity swiftly recovers to 1085 mAh g⁻¹ when the current density is restored to 0.1 A g⁻¹, indicating good reversibility and robustness of the composite. Additionally, the long-term cycling performance and the corresponding coulombic efficiency of the CoFe₂O₄/GAs composite at a current density of 0.5 A g⁻¹ are shown in Fig. 5e. It is obvious that the reversible lithium storage capacity for CoFe₂O₄/GAs electrode decays before 100 cycles and then gradually increases in the following cycles. The charge capacity reaches up to 966 mAh g⁻¹ after 300 cycles, with the coulombic efficiency 99.5%. The similar phenomenon that the reversible capacity of transition metal oxide electrode increases during cycling has been reported in previous studies.⁴⁸ The possible reason would be the electrode activation process.

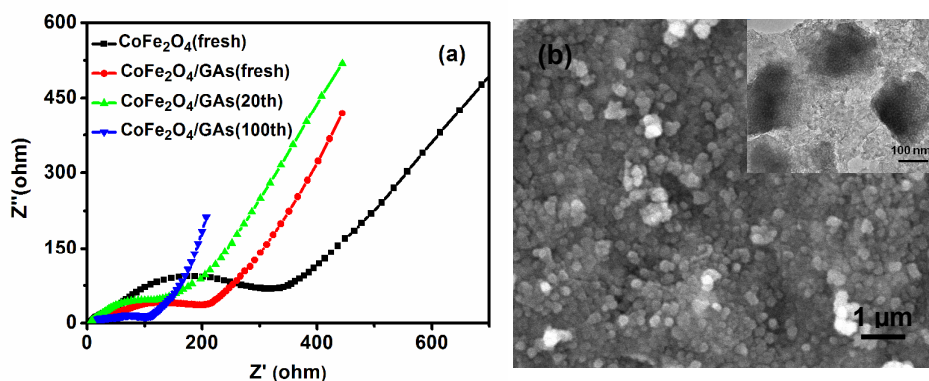


Fig. 6 (a) Nyquist plots of CoFe₂O₄/GAs electrode at different states of discharge/charge cycling, and (b) SEM image of the CoFe₂O₄/GAs electrode after 100 cycles at a current density of 0.1 A g⁻¹. Inset of (b) shows the TEM image of the CoFe₂O₄/GAs electrode after 100 cycles.

To gain insight into the reason why CoFe₂O₄/GAs electrode displays such excellent performance compared to pure CoFe₂O₄ electrode, EIS analysis was carried out at room temperature in the frequency range of 0.01 Hz to 100 kHz. The Nyquist plots of the CoFe₂O₄/GAs and CoFe₂O₄ electrodes before cycling are shown in Fig. 6a. All impedance spectra consist of a single semicircle in the high-middle frequency region and a sloping line in the low-frequency region, representing the charge-transfer impedance in the electrode/electrolyte and lithium-diffusion process of the electrodes. It is clearly seen that the diameter of the semicircle in the high-middle frequency region for the CoFe₂O₄/GAs electrode before cycling is smaller than that of pure CoFe₂O₄ electrode, indicating that the CoFe₂O₄/GAs electrode possess a lower contact and charge-transfer resistance. On the other hand, the EIS profile of CoFe₂O₄/GAs electrode before cycling exhibits a higher low-frequency slope angle compared with that of CoFe₂O₄ electrode, indicating faster lithium-diffusion process of the CoFe₂O₄/GAs electrode. On the basis of the above result, the GAs can greatly improve the electrical conductivity of the CoFe₂O₄/GAs electrode and help to decrease the charge-transfer resistance, resulting in significant improvement in the cycling and rate performance. In addition, the diameter of the semicircle in the high-middle frequency region is decrease with increasing cycle number, revealing the existence of the activating process of the electrode during repeated lithium insertion/extraction processes.⁴⁹ The results indicate that CoFe₂O₄/GAs electrode exhibits excellent electrochemical performance as anode material for LIBs. Meanwhile, SEM and TEM images of the CoFe₂O₄/GAs electrode after 100 cycles at a constant current density of 0.1 A g⁻¹ are shown in Fig. 6b. It is obvious that the structure of the CoFe₂O₄/GAs electrode still maintains its original structure, highlighting the stability of the unique structure. These results demonstrate that the

3D GAs can effectively accommodate the strain of volume change and suppress the agglomeration of the CoFe_2O_4 during cycling, which consequently enhances the cyclic stability and rate capability.

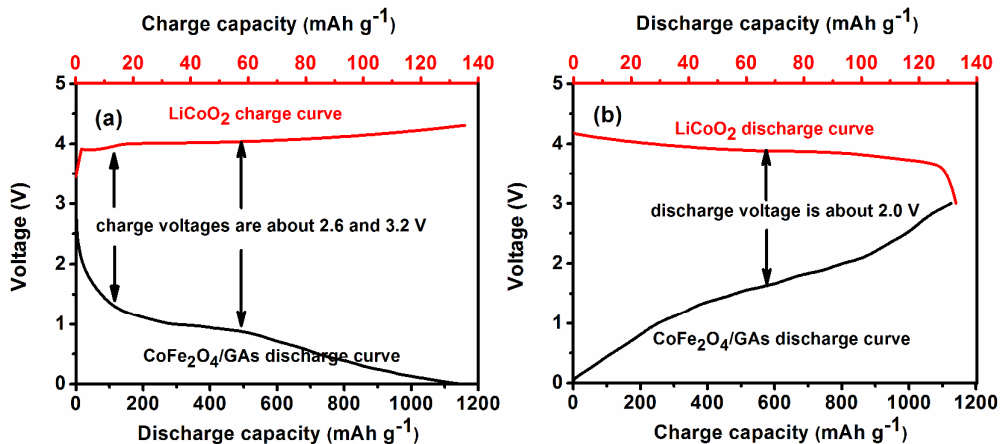


Fig. 7 (a) The charge (LiCoO_2 electrode in half-cell, upper) and discharge ($\text{CoFe}_2\text{O}_4/\text{GAs}$ electrode in half-cell, lower) curves. (b) The discharge (LiCoO_2 electrode in half-cell, upper) and charge ($\text{CoFe}_2\text{O}_4/\text{GAs}$ electrode in half-cell, lower) curves.

To evaluate the practical performance of $\text{CoFe}_2\text{O}_4/\text{GAs}$ composite in commercial batteries, full cell was assembled by using the commercial LiCoO_2 as the cathode and $\text{CoFe}_2\text{O}_4/\text{GAs}$ as the anode. The discharge curve of the $\text{CoFe}_2\text{O}_4/\text{GAs}$ anode and the charge curve of the LiCoO_2 cathode in their respective half cells are shown in Fig. 7a. And Fig. 7b displays the charge curve of $\text{CoFe}_2\text{O}_4/\text{GAs}$ anode and the discharge curve of the LiCoO_2 cathode in their respective half cells. According to the results obtained in Fig. 7, the charge voltage plateaus of $\text{CoFe}_2\text{O}_4/\text{GAs}/\text{LiCoO}_2$ full cell should be about 2.6 and 3.2 V, while the discharge voltage plateau is about 2.0 V. Therefore, we designed that the practical working voltage of the $\text{CoFe}_2\text{O}_4/\text{GAs}/\text{LiCoO}_2$ full cell ranges between 1 and 3.8 V for different current densities.

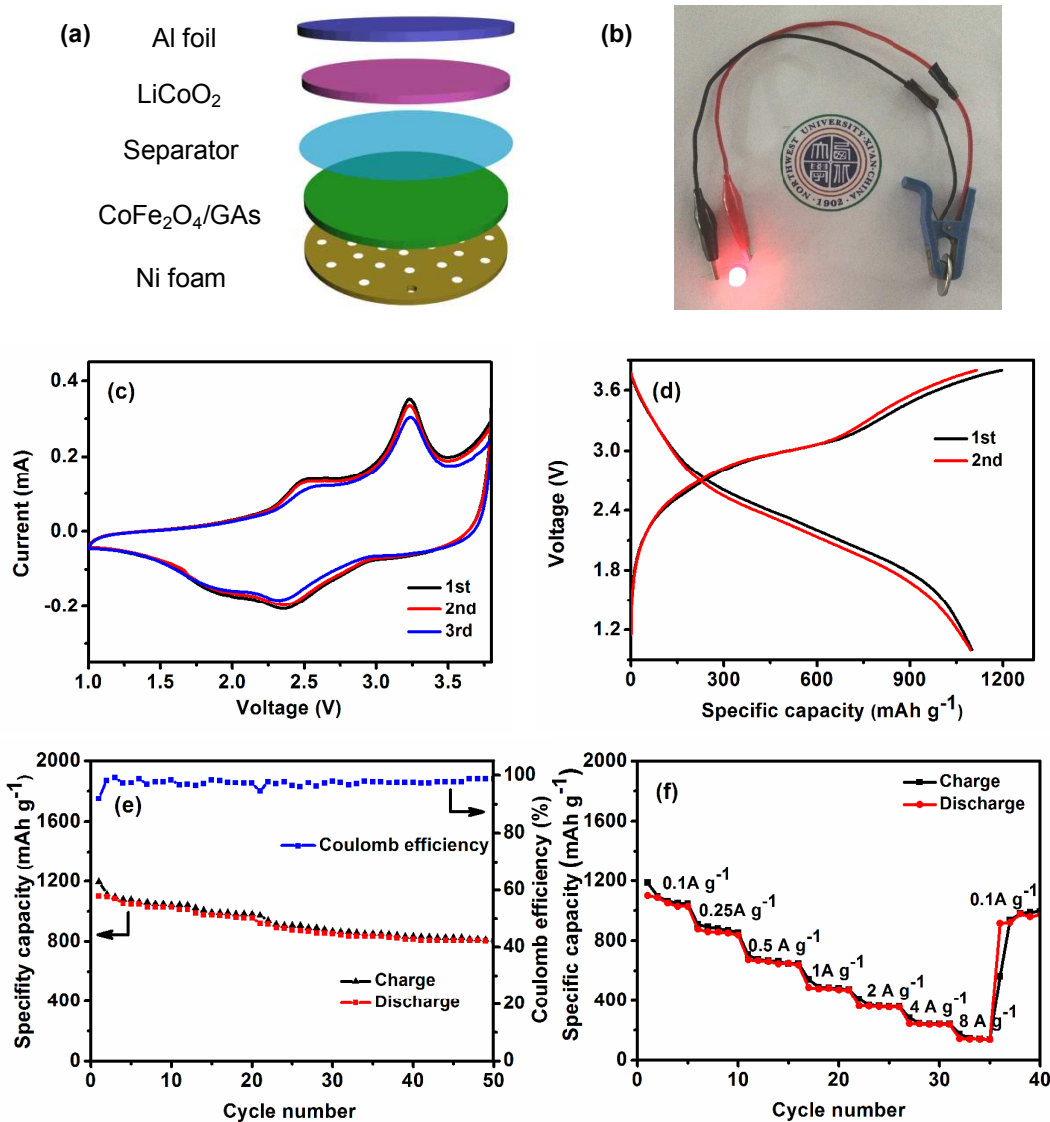


Fig. 8 (a) Schematic of the CoFe₂O₄/GAS//LiCoO₂ full-cell. (b) Digital image of a light-emitting diode lit by the CoFe₂O₄/GAS//LiCoO₂ full-cell. (c) CV profiles of the initial three cycles for the CoFe₂O₄/GAS//LiCoO₂ full-cell. (d) Charge and discharge profiles of the CoFe₂O₄/GAS//LiCoO₂ full-cell. (e) Cycle performance and coulombic efficiency of the CoFe₂O₄/GAS//LiCoO₂ full-cell. (f) Rate performance of the CoFe₂O₄/GAS//LiCoO₂ full-cell at various rates.

Fig. 8a shows the structure of an assembled full-cell with CoFe₂O₄/GAS anode and LiCoO₂ cathode. The digital image of a light-emitting-diode (LED) lighting by the

CoFe₂O₄/GAs//LiCoO₂ full cell is shown in Fig. 8b. To avoid the large capacity loss during the first charge process in full cell, the CoFe₂O₄/GAs electrode is electrochemically activated for three cycles in a half cell at a current rate of 0.1 A g⁻¹. The full cell was slightly anode limited and was cycled at a current density of 0.1 A g⁻¹ (based on the anode weight). The CV curves of CoFe₂O₄/GAs//LiCoO₂ full cell in the first three cycles are shown in Fig. 8c at a scanning rate of 0.1 mV s⁻¹. In the first cycle, two peaks at 2.5 and 3.2 V appear in anode scan and one broad peak at 1.7~2.4 V in cathodic scan. In the following cycles, no obvious potential shift can be found in these peaks. The CV curve shape of CoFe₂O₄/GAs//LiCoO₂ full cell is consistent with that of the CoFe₂O₄/GAs anode half cell. Fig. 8d reveals the representative charge/discharge voltage profiles of the CoFe₂O₄/GAs//LiCoO₂ full cell. The corresponding two charge plateaus at 2.7 and 3.2 V and a broad discharge plateau at about 2.4~1.8 V are observed during the lithium insertion/extraction processes, which agree well with the CV results. The cycling performance and the corresponding coulombic efficiency of CoFe₂O₄/GAs//LiCoO₂ full cell are shown in Fig. 8e. The first charge/discharge capacities are 1197 mAh g⁻¹ and 1100 mAh g⁻¹ (based on the active mass of the CoFe₂O₄/GAs electrode), with a coulombic efficiency of 92%. The irreversible capacity loss may be due to SEI film formation at the LiCoO₂ cathode side in the first charge process. It is noted that the reversible capacity slowly reduces to 803 mAh g⁻¹ in the 50th cycle, whereas the coulombic efficiency increases to 99%. The rate performance of the CoFe₂O₄/GAs//LiCoO₂ full cell from 0.1 to 8 A g⁻¹ was tested, as shown in Fig. 8f. The discharge capacities of CoFe₂O₄/GAs//LiCoO₂ full cell are about 881, 666, 492, 368, 246 and 146 mAh g⁻¹ at current densities of 0.2, 0.5, 1, 2, 4 and 8 A g⁻¹, respectively. It can be seen that the electrode recovers the capacity and reaches nearly 978 mAh g⁻¹, when the current density is returned to the initial 0.1

A g^{-1} , indicating the good rate capability and stability of the electrode material. Considering the favorable operation of $\text{CoFe}_2\text{O}_4/\text{GAs}$ in the full cell system, it is believed the composite may have potential application in commercial LIBs.

4. Conclusions

We have developed a simple and scalable method to prepare novel and unique $\text{CoFe}_2\text{O}_4/\text{GAs}$ composite as an anode material for LIBs. The GAs as an underlying substrate can not only effectively prevent the aggregation of CoFe_2O_4 , but also provide excellent flexibility and elasticity to accommodate the mechanical stress caused by the volume change during the discharge and charge processes. Meanwhile, the hierarchical CoFe_2O_4 nanoclusters uniformly encapsulated in GAs can suppress the stacking of the neighboring graphene sheets. Benefiting from this remarkable synergy, the $\text{CoFe}_2\text{O}_4/\text{GAs}$ electrode exhibits high specific capacity, excellent cycling stability and superior rate capabilities in both half and full cell systems. We believe that the novel and simple preparation method introduced here could be extended to design other ternary iron oxides/GAs composites.

Acknowledgements

This work was supported by the financial supports of the National Natural Science Foundation of China (Nos. 21301140 and 21061130551) and Northwest University Cross-discipline Fund for Postgraduate Students (YZZ14008).

References

- 1 M. Armand, J. M. Tarascon, Building better batteries, 2008, **451**, 652.
- 2 I. Kovalenko, B. Zdyrko, A. Magasinski, B. Hertzberg, Z. Milicev, R. Burtovyy, I. Luzinov, G. Yushin, Science, 2011, **334**, 75.
- 3 X.L. Huang, R.Z. Wang, D. Xu, Z.L. Wang, H.G. Wang, J.J. Xu, Z. Wu, Q.C. Liu, Y. Zhang and X.B. Zhang, Adv. Funct. Mater., 2013, **23**, 4345.

- 4 G.X. Gao, H.B. Wu , B.T. Dong , S.J. Ding , and X.W. (David) Lou, *Adv. Sci.*, 2015, **2**, 1400014.
- 5 B.B. Wang, G. Wang, Z.Z. Zheng, H. Wang, J.T. Bai , J.B. Bai, *Electrochim. Acta*, 2013, **106**, 235.
- 6 Z. Bai, Z. Ju, C. Guo, Y. Qian, B. Tang and S. Xiong, *Nanoscale*, 2014, **6**, 3268.
- 7 H. Song, L. Shen and C. Wang, *J. Mater. Chem. A*, 2014, **2**, 20597.
- 8 G.D. Park and Y.C. Kang, *Chem.-A Eur. J.*, 2015, **2**, 9179.
- 9 J.X. Guo, B. Jiang, X. Zhang, L. Tang and Y.H. Wen, *J. Mater. Chem. A*, 2015, **3**, 2251.
- 10 Y. Ding, Y. Yang, H. Shao, *J. Power Sources*, 2013, **244**, 610.
- 11 Z. Xing, Z. Ju, J. Yang, H. Xu, Y. Qian, *Electrochim. Acta*, 2013, **102**, 51.
- 12 Y.C. Dong, Y. Xia, Y.S. Chui, C.W. Cao, Juan Antonio Zapien, *J. Power Sources*, 2015, **275**, 769.
- 13 Z.H. Li, T.P. Zhao, X.Y. Zhan, D.S. Gao, Q.Z. Xiao, G.T. Lei, *Electrochim. Acta*, 2010, **55**, 4594.
- 14 D. Gu, W. Li, F. Wang, H. Bongard, B. Spliethoff, W. Schmidt, C. Weidenthaler, Y.Y. Xia, D.Y. Zhao, and F. Schîth, *Angew. Chem. Int. Ed.*, 2015, **54**, 7060.
- 15 Z.H. Li, T.P. Zhao, X.Y. Zhan, D.S. Gao, Q.Z. Xiao and G.T. Lei, *Electrochim. Acta*, 2010, **55**, 4594.
- 16 X.Y. Yao, J.H. Kong, X.S. Tang, D. Zhou, C.Y. Zhao, R. Zhou and X.Y. Lu, *RSC Advance*, 2014, **4**, 27488
- 17 Z.L Zhang, Y.H. Wang, M.J. Zhang, Q.Q. Tan, X. Lv, Z.Y. Zhong and F.B. Su, *J. Mater. Chem. A*, 2013, **1**, 7444.
- 18 X. Zhang, Y.P. Xie, Y.F. Sun, Q. Zhang, Q.Y. Zhu, D. Houa and J.X. Guo, *RSC Advance*, 2015, **5**, 29837.

- 19 N.N. Wang, H.Y. Xu, L. Chen, X. Gu, J. Yang and Y.T. Qian, *J. Power Sources*, 2014, **247**, 163.
- 20 S.Y. Liu, J. Xie, C.C. Fang, G.S. Cao, T.J. Zhu and X.B. Zhao, *J. Mater. Chem.*, 2012, **22**, 19738.
- 21 Y.J. Chen, J. Zhu, B.H. Qu, B.A. Lu, Z. Xu, *Nano Energy*, 2014, **3**, 88.
- 22 G.X. Gao, H.B. Wu, X.W. Lou, *Adv. Energy Mater.*, 2014, **4**, 1400422.
- 23 I. Nam, N.D. Kim, G.P. Kim, J. Park, J. Yi, *J. Power Sources*, 2013, **244**, 56.
- 24 H.Y. Wang, B.Y. Wang, J.K. Meng, J.G. Wang and Q.C. Jiang, *J. Mater. Chem. A*, 2015, **3**, 1023.
- 25 A.K. Rai, T.V. Thi, B.J. Paul, J. Kim, *Electrochim. Acta*, 2014, **146**, 577.
- 26 J.X. Guo, B. Jiang, X. Zhang, H.T. Liu, *J. Power Sources* 2014, **262**, 15.
- 27 J.X. Guo, F.F. Li, J. Sui, H.F. Zhu, X.Zhang, *Ionics* 2014, **20**, 1635.
- 28 Z.S. Wu, Y. Sun, Y.Z. Tan, S.B. Yang, X.L. Feng, K. Müllen, *J. Am. Chem. Soc.*, 2012, **134**, 19532.
- 29 J.P. Zhao, S.F. Pei, W.C. Ren, L.B. Gao, and H.M. Cheng, *ACS Nano*, 2010, **4**, 5245.
- 30 H. Xia, D.D. Zhu, Y.S. Fu, X. Wang, *Electrochim. Acta*, 2012, **83**, 166.
- 31 J.Y. Yao, Y.J. Gong, S.B. Yang, P. Xiao, Y.H. Zhang, K. Keyshar, G.L. Ye, S. Ozden, R. Vajtai, and P.M. Ajayan, *ACS Appl. Mater. Interfaces*, 2014, **6**, 20414.
- 32 L. Xiao, D.Q. Wu, S. Han, Y.S. Huang, S. Li, M.Z. He, F. Zhang and X.L. Feng, *ACS Appl. Mater. Interfaces*, 2013, **5**, 3764.
- 33 Z.Y. Zhang, W.Y. Li, R.J. Zou, W.P. Kang, Y.S. Chui, M.F. Yuen, C.S. Lee and W.J. Zhang, *J. Mater. Chem. A*, 2015, **3**, 6990.
- 34 N. Li, M. Zheng, X. Chang, G. Ji, H. Lu, L. Xue, L. Pan, J. Cao, *J. Solid State Chem.*, 2011, **184**, 953.

- 35 Y.C. Dong, Y.S. Chui, X. Yang, R.G. Ma, J.M. Lee, and J.A. Zapien, *ChemElectroChem*, 2015, **2**, 1010.
- 36 Z. H. Li, T.P. Zhao, X.Y. Zhan, D.S. Gao, Q.Z. Xiao, G.T. Lei, *Electrochim. Acta*, 2010, **55**, 4594.
- 37 B.B. Wang, G. Wang, H. Wang, *J. Mater. Chem. A*, 2015, **3**, 17403.
- 38 Y.L. Xiao, J.T. Zai, L.Q. Tao, B. Li, Q.Y. Han, C. Yu and X.F. Qian, *Phys. Chem. Chem. Phys.*, 2013, **15**, 3939.
- 39 Y.B. Lou, J. Liang, Y.L. Peng and J.X. Chen, *Phys. Chem. Chem. Phys.*, 2015, **17**, 8885.
- 40 L.S. Fan, B.J. Li, D.W. Rooney, N.Q. Zhang and K.N. Sun, *Chem. Commun.*, 2015, **51**, 1597.
- 41 S.H. Ren, X.Y. Zhao, R.Y. Chen, M. Fichtner, *J. Power Sources*, 2014, **260**, 205.
- 42 H. Fu, Z.J. Du, W. Zou, H.Q. Li, C. Zhang, *Carbon*, 2013, **65**, 112.
- 43 J.W. Xiao, G.L. Xu, S.G. Sun and S.H. Yang, *Part. & Part. Syst. Char.*, 2013, **30**, 893.
- 44 M. Zhang, X. Yang, X.F. Kan, X. Wang, L. Ma, M.Q. Jia, *Electrochim. Acta*, 2013, **112**, 727.
- 45 T. Sener, E. Kayhan, M. Sevim, O. Metin, *J. Power Sources*, 2015, **288**, 36.
- 46 P.R. Kumar, P. Kollu, C. Santhosh, K.E.V. Rao, D.K. Kim and A.N. Grace, *New J. of Chem.*, 2014, **38**, 3654.
- 47 J.J. Zhou, T. Yang, M.L. Mao, W.J. Rena and Q.H. Li, *J. Mater. Chem. A*, 2015, **3**, 12328.
- 48 M. Bijelic, X. Liu, Q. Sun, A.B. Djurić, M.H. Xie, A.M.C. Ng, C. Suchomski, I. Djerdj, Z. Skokoć and J. Popovic, *J. Mater. Chem. A*, 2015, **3**, 14759.
- 49 Y. Liu, X.G. Zhang, *Electrochim. Acta*, 2009, **54**, 4180.